Datashare 140

Low pressure buildup with large disposal volumes of oil field water: A flow model of the Ellenburger Group, Fort Worth Basin, northcentral Texas

Shuang Gao, Jean-Philippe Nicot, Peter H. Hennings, Paul La Pointe, Katie M. Smye, Elizabeth A. Horne, and Robin Dommisse

AAPG Bulletin, v. 105, no. 12 (December 2021), pp. 2575–2593

INTRODUCTION

This file includes additional data complementing model building description as presented in the main text.

Section A gives a narrative of minor input parameters and justifications for their choice.

Section B presents a detailed analysis on how stochastic and framework fault properties were derived using published literature and data, fit-for-purpose field data collected during the study, and two well tests.

Section C describes how porosity and permeability fields were implemented into the model from information presented in Section B and well logs.

Section D details an important aspect of the conceptual model, that is, a nonnegligible fraction of the water produced through Barnett wells is withdrawn from the Ellenburger (and then reinjected into the Ellenburger through the disposal wells).

Section E discusses the calibration approach and results.

Section F considers these sensitivity analysis results not discussed in the main text.

A reference list is appended at the end of the document.

A. MODEL INPUT AND MODELING DETAILS

Validity of Darcy's Law in a Fractured System

The modeling approach chosen is very simple in principle and relies on the straightforward application of Darcy's law in a single-phase flow system with no attempt made to include the possible effect of poroelasticity, which has been shown to have a small effect on the possible change in pore pressure of the Ellenburger Group (EBG) in the Fort Worth Basin (FWB) (Zhai and Shirzaei, 2018). The validity of using a simple Darcian model could be questioned given the karstic, faulted, and fractured nature of the system. However, use of such models is not uncommon (e.g., Scanlon et al., 2003; Shi et al., 2016) and is generally accepted as valid for regional models. Furthermore, assuming the high-case scenario of an injection rate of 50,000 bbl/day (92 L/s) directly into a 300-ft (100-m)-high conduit section yields a Reynolds number (*Re*) slightly below 2000. Although this *Re* value is typically seen as the upper bound for laminar flow, which is then nonlinear and non-Darcian, it can be overlooked because the model has, by construction, no well injecting directly into a framework fault.

Southern Boundary at EBG Outcrop

The southern boundary is downdip of the main groundwater circulation area away from outcrops of the Cambrian–Ordovician on the Llano Uplift of central Texas (Standen and Ruggiero, 2007). Cambrian clastic formations and the EBG are productive freshwater aquifers that have short travel paths from recharge to discharge into rivers and therefore contribute little recharge to the deeper principal model domain at the time scale of the model. The assumption can be justified by a simple calculation. For example, deep recharge of 0.1% of the annual rainfall of 30 in./yr (e.g., Huang et al., 2012; Shi et al., 2016) over the ~2000 km^2 of EBG outcrop translates into ~30,000

bbl/day, similar to the rate of one high-volume SWD well. In addition, the assumption of a no-flow boundary in the south is further justified by the great lateral distance from the main injection and production areas.

Pressure Distribution

The system is assumed to be normally pressured as suggested by pressure measurements presented in Figure S1A.

Bottom Boundary

A no-flow boundary is placed within the basement at the bottom of the model at 2000 ft (610 m) below the contact of the basement and sediments above, thereby mirroring the shape of the Cambrian unconformity. This boundary is predicated on the observation from petroleum and groundwater reservoirs in crystalline and metamorphic basement globally where the permeability, in otherwise very low permeability rock, is enhanced by alteration and fractures (Cuong and Warren, 2009). The distribution of basement rock types in the FWB is not known. The seven wells that we have been able to identify in the area of interest (AOI) that penetrate basement and have log data available suggest a mix of granitic and metamorphic lithologies (Smye et al., 2019). These rocks appear similar to the outcrops of basement in central Texas (Setlur et al., 2019).

Conventional Oil and Gas Production from EBG

There is minor conventional production from EBG wells in the northern and western margins of the model. There, most of the produced water is reinjected for pressure control and the total hydrocarbon production is dwarfed by the disposal volumes studied here. Available data suggest that <50 million bbl of oil and <60 BCF (1.7×10^9 m^3) of (mostly solution) gas have been produced from the 1950s in Archer, Clay, Jack, and Montague Counties (~50% of total) and in counties forming the western limit of the model (mostly in Callahan, Eastland, and Shackelford Counties). Production has considerably waned since its 1980s peak, but cumulatively produced and subsequently reinjected water volume is in the order of <300 million bbl, which represents a reasonably high water cut of ~85% in par with mature conventional wells. In addition, there is very minor historical gas production (~2 BCF [57×10^6 m^3]) from the EBG in south Wise County and across the Wise-Parker County line, much closer to the dense injection areas, but overall very few gas shows in the EBG. Large gas accumulations would have a large impact on the bulk compressibility of the system and could cushion any pressure increase in their vicinity.

Formation Compressibility

Base case pore compressibility of the rock formations (with *bulk compressibility* = *porosity compressibility* × *porosity*) was estimated at the reference value of 8.27×10^{-6} psi^{-1} (1.20 GPa^{-1}) for EBG layers, that is, a bulk compressibility of 0.25×10^{-6} psi^{-1} (0.04 GPa^{-1}) based on a 3% average porosity; this value is consistent with published data (e.g., 9.5×10^{-6} psi^{-1} to 1.38 GPa^{-1} from Hall, 1953; 8.25×10^{-6} psi^{-1} to 1.20 GPa^{-1} from Railroad Commission of Texas, 2015c) and data computed from well logs in the EBG such as 8.67×10^{-6} psi^{-1} (1.26 GPa^{-1}) extracted from petrophysical data in Waters et al. (2011) and averaged values extracted from Railroad Commission of Texas (RRC) files: 1.7~10.7, averaged at 3.7, 3.7×10^{-6} psi^{-1} (0.54 GPa^{-1}) from well 1 (API 42-367-33362) and 6~19, averaged at 11.5, 11.5×10^{-6} psi^{-1} (1.67 GPa^{-1}) from well 2 (API 42-439-31781). Basement pore compressibility is estimated at the value of 27.6×10^{-6} psi^{-1} (4.1 GPa^{-1}), that is, a bulk compressibility of 0.14×10^{-6} psi^{-1} (0.02 GPa^{-1}) consistent with published data (e.g., 0.1379×10^{-6} psi^{-1} (0.02 GPa^{-1}) from Brace et al., 1968) and extracted from Waters et al. (2011) at 0.197×10^{-6} psi^{-1} (0.03 GPa^{-1}).

Salinity Distribution

The salt content of the resident water (total dissolved solids [TDS]) is variable from brackish to very saline (>250,000 mg/L) (Figure S1B). The most complete TDS data set of deep sections of the EBG in the FWB is old (Texas Water Development Board, 1972), with a total of ~80 data points, half of which comes from actual chemical analyses and the other half from estimates from well-log interpretation. The exact depth of the samples is generally not known. However, the salinity distribution is assumed to be depth-stratified, particularly, close to northeast corner of

the model where the basin is deepest, although in the details, the highest TDSs may not fully coincide with the deepest basement tops. A relevant feature of the TDS spatial distribution is a much smaller gradient in the southwest-northeast direction along the structural grain than in the perpendicular direction. Past recharge from the Llano uplift might be responsible for this pattern. The fact that the current distribution is not radial out of the uplift strongly suggests a preferential flow to the northeast along the main structural direction. Water is modeled as a fluid with two components, a water at 1000 mg/L and a water at 280,000 mg/L. Initial salinity and produced water injection stream are modeled as containing fractions of these two components.

Salinity of Injection Stream

Average TDS of the injected water is uncertain, operational practices (hydraulic fracturing [HF] stimulation done with fresh water, Nicot et al., 2014) and sparse produced water measurements (Nicot, unpublished data) supported by external references (Kondash et al., 2017) suggest a value of ~80,000 mg/L, which is lower than the TDS of the resident water. A second justification for the lower TDS is smectite-to-illite conversion, hypothesized by some authors, that could decrease the TDS in the deeper sections of the Barnett as observed in the Eagle Ford Shale and the Permian Basin (Nicot et al., 2018). A simple calculation suggests that each injection well receives produced water from 50 to 200 producing wells (average and median distance between a Barnett well and the closest disposal well are in the 3.5–4-mi range [~6 km]).

Temperature Distribution

The geothermal gradient varies laterally and vertically, but we adopted an averaged geothermal

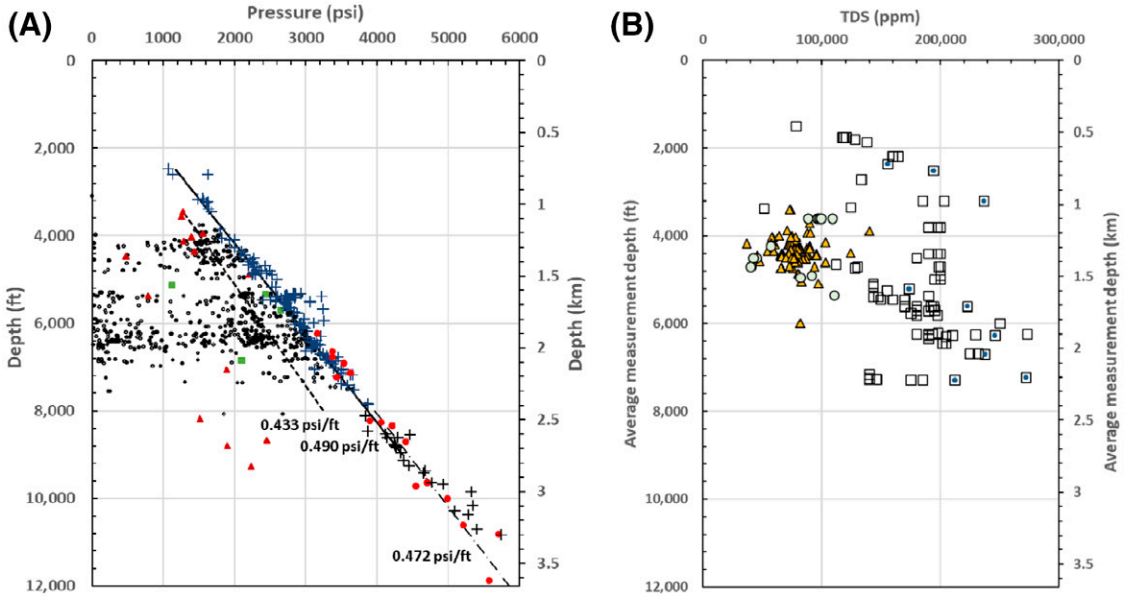

Figure S1. (A) Bottomhole pressure measurements (1 MPa = 145 psi) from injection wells located in Johnson and Tarrant Counties (red circles). Pressure measurements collected from the IHS database (388 wells); solid circles: Drill stem test initial shut-in pressure; open circles: final shut-in pressure, triangles: maximum of tubing shut-in pressure and so-called bottomhole pressure of production tests; squares: from instantaneous shut-in pressure during treatment assuming a Poisson's ratio of 0.25; "+" indicates pressure computed from mud weight. The pressure gradient is very variable depending of the location, high at the northern boundary where the total dissolved solid (TDS) is the highest and low on the western boundary where total dissolved solids TDS tend to be lower. The Ellenburger Group section of the Fort Worth Basin is normally pressured with a variable pressure gradient depending on the local TDS. (B) Salinity measurements; squares: northern section of the model along the Muenster arch, TDS is high even at shallow depths toward the western edge of the model; triangles: in the western half of the model; circles: south of the model north of the Llano uplift. Data points correspond to locations of conventional production in the northern and western sections of the models. Ellenburger Group in the core area and area of interest have been seldom sampled, but the local pressure gradients suggest TDS is lower than in the northern section along the Muenster arch.

gradient of 1.6°F/100 ft (29.2°C/km) (Texas Water Development Board, 1972), consistent with 73 measured bottomhole temperature (IHS Markit). Initial temperature of the system follows this generalized gradient with a generalized surface temperature of 68°F (20°C). The temperature in the model ranges from approximately surface temperature to ~300°F (~150°C). It is assumed that the injected water, at 68°F (20°C), is immediately in thermal equilibrium with the resident water of the various cells it is injected into. Fluid and rock temperatures are strictly a function of depth only but do impact flow through variable water density and viscosity.

B. IMPLEMENTATION OF ANISOTROPIC AND HETEROGENEOUS PERMEABILITY FROM STOCHASTIC ANALYSIS AND MODELING

B.1. Development and Upscaling of Discrete Fracture Network Models for the FWB Fault System

Smaller faults that are not easily detected through seismic data are widespread throughout the basin and contribute to formation permeability. The additional permeability and porosity provided by these faults were estimated through discrete fracture network (DFN) modeling (La Pointe and Lim, 2018, personal communication). This was performed to (1) assess areas of the model with poor controls on faults can be populated stochastically with information from areas of the model with better data availability and (2) implement reasonable ranges of fault permeability and porosity values that can be upscaled to the flow model. As described in Horne et al. (2020), information on fault existence and characteristics is available in areas of the basin where there is control from outcrops, vertical and horizontal wells, two-dimensional and three-dimensional (3-D) reflection seismic data, and interpretations of earthquake hypocenters. For the DFN modeling, this interpretation consisted of 111 framework-scale (tectonic) faults in the basin, 1654 faults from published geologic maps in the Llano uplift, and small faults collected from outcrops of the EBG in the Llano uplift (Figure 3). The fault information derived from these sources was not uniform in spatial coverage, resolution, or detection reliability, and so the various data sets were tested for consistency. Key parameters needed for the FWB stochastic fault model were orientation, intensity, spatial location, size and shape (trace length and height), hydraulic aperture, and permeability. As described in Section B.2, public domain data from two wells in the basin adjacent to faults provided transient well tests that could be used to estimate directional fracture network permeability and fracture porosity for the EBG rock volume.

The first step in constructing DFN fault models is to develop a quantitative statistical parameterization of the geometry (orientation, area, shape), spatial intensity and hydraulic properties (intrinsic permeability, aperture and compressibility) of the faults in the DFN model. The outcrop data are measured with high resolution and provide detailed and consistent parameterization of the fault geometric information (Horne et al., 2020). For the outcrop areas, fault intensity, representing the deformation intensity in the system, is specified with total fracture surface area per unit volume of rock, or volumetric intensity P_{32} (Dershowitz and Herda, 1992). The linear fracture intensity P_{10} is measured as number of fractures per unit length of an imaginary line affixed to the middle of the outcrop face. The DFN simulation model used measured fault orientations and heights and adjusted volumetric intensity P_{32} until the modeled linear fault intensity P_{10} matched with measurement.

The large-scale fault strikes are preferentially southwest-northeast, although there is some variation especially in the northeast section of the basin (Figure 3). Dips range from 60° to 80° (average 72°) in general to the northwest. A secondary set oriented northwest-southeast may create a connected fracture network when combined with the primary set. The geometric parameters from outcrops were found to be consistent with subsurface fault properties derived from 3-D reflection seismic data (Hardage et al., 1996; McDonnell et al., 2007; Elebiju et al., 2010; Khatiwada et al., 2013) and published data sets (Kier et al., 1976; Barnes and Rose, 1981; Ewing, 1991). Figure S2 shows an example of the orientation consistency among different regions of the basin and among different data sources, whereas Figure S3 shows consistency is size and intensity. The consistency across the basin suggests that all data can be combined and used to build a statistically homogeneous (at least on a coarse scale) basin-wide DFN, as well as to populate volumes with limited or no published or measured fault data. This

statistical consistency, including the fault data update by Hennings et al. (2019), suggests that faults originated because of tectonic processes operating at least at the scale of the FWB. This is particularly evident in the orientations of faults in the Llano uplift area, which maintain their northeast strikes rather than forming concentric or radial patterns around the uplift.

B.2. Calibration of Porosity and Permeability of FWB Faults and Fractures

Results from two pump tests are used to anchor the porosity and permeability distributions, as well as to build confidence in the geometrical parameterization of the DFN fault model. A series of felt earthquakes caused the Texas RRC to require additional studies of several wells that provides data that are generally not collected or not in the public domain but now available from court dockets (one near Venus fault group in the Venus earthquake area in Johnson County, and another near Azle fault group in the Azle-Reno earthquake area) in Wise, Parker, and Tarrant Counties. In particular, to derive properties for fracture aperture, fracture permeability and fracture compressibility, dynamic tests are simulated using local DFN fault models consistent with specific fault data from the areas of the well tests (Figure 3): HWY67 injection well HWY67: EnerVest and Briar well No. 1 injection well Briar1: Pinnergy (RRC, 2015a, b). In this approach, starting values for fault aperture (e), fault permeability (kf), and fault compressibility (Cf) are assigned, along with representative matrix permeability and porosity values. Values of e, kf, and Cf are then varied within reasonable constraints to obtain as close a match as possible to the observed well test data. Figure S4 shows the final match between the DFN model and the Briar1 test data. The fault aperture × intrinsic permeability product (kh) values for these two tests are very similar: 8450 md-ft and 7249 md-ft for the HWY67 and Briar1 tests, respectively. Although the actual fault aperture and intrinsic permeability values used in the matching of these two tests differed significantly, the calculation of the upscaled fault permeability only depends upon kh. The kh values obtained from the HWY67 and Briar1 wells, which are located in separate counties in the FWB, suggest that they are representative of the EBG in the basin where it is similarly faulted. These data form the base case for fault kh in the basin.

B.3. Populating *kh* Using DFN Modeling

Distributing fault kh throughout the model followed two additive steps. The first step includes only what is known deterministically with a high degree of confidence and therefore includes only the large faults in the subsurface of the basin (Horne et al., 2020). The second step adds to the smaller faults that occur throughout the FWB which were implemented stochastically (Figure S5).

In the first step, all faults were assigned an aperture (0.005 ft [1.5 mm]) and permeability of 1.0×10^9 md based on the Briar1 well test matching results (Figure S6). The fault directional permeability and porosity were upscaled using the algorithms developed by Oda (1985). The upscaled permeability is horizontally anisotropic, with the I-grid direction (northwest) being lower than the J-grid direction (northeast). The vertical upscaled permeability is similar to the J-direction permeability. Fault porosity is explicitly modeled in the cells with major faults and can be as low as 0.002%. In this model, very little pore volume is provided by the fault system, although the permeability is greatly enhanced.

The second step is to estimate the permeability and porosity created by the faults that are not part of the framework fault set. This was done by creating a stochastic DFN model for these faults using the geometric and hydraulic parameterization previously described. These faults are conceptualized as secondary faults formed around the larger framework faults and, as such, have orientations similar to the adjacent framework faults and intensity that decreases with distance from the faults. These assumptions extend the presence of faults away from the large-scale faults and leads to faults of much smaller scale occurring throughout the FWB, as is clearly observed in the outcrop fault data.

As a consequence of this conceptual model, the orientations of the stochastic faults were spatially bootstrapped from the orientations of the framework faults using an inverse-distance-square weighting function. Note how the orientations of the stochastic faults in Figure S5 tend to follow the orientations of the nearby framework faults.

The stochastic fault intensity was based upon an estimated fault heave. Estimated fault heave, normalized to a range of 0.0 to 1.0 for modeling purposes, is shown in Figure S7A. The volumetric fracture

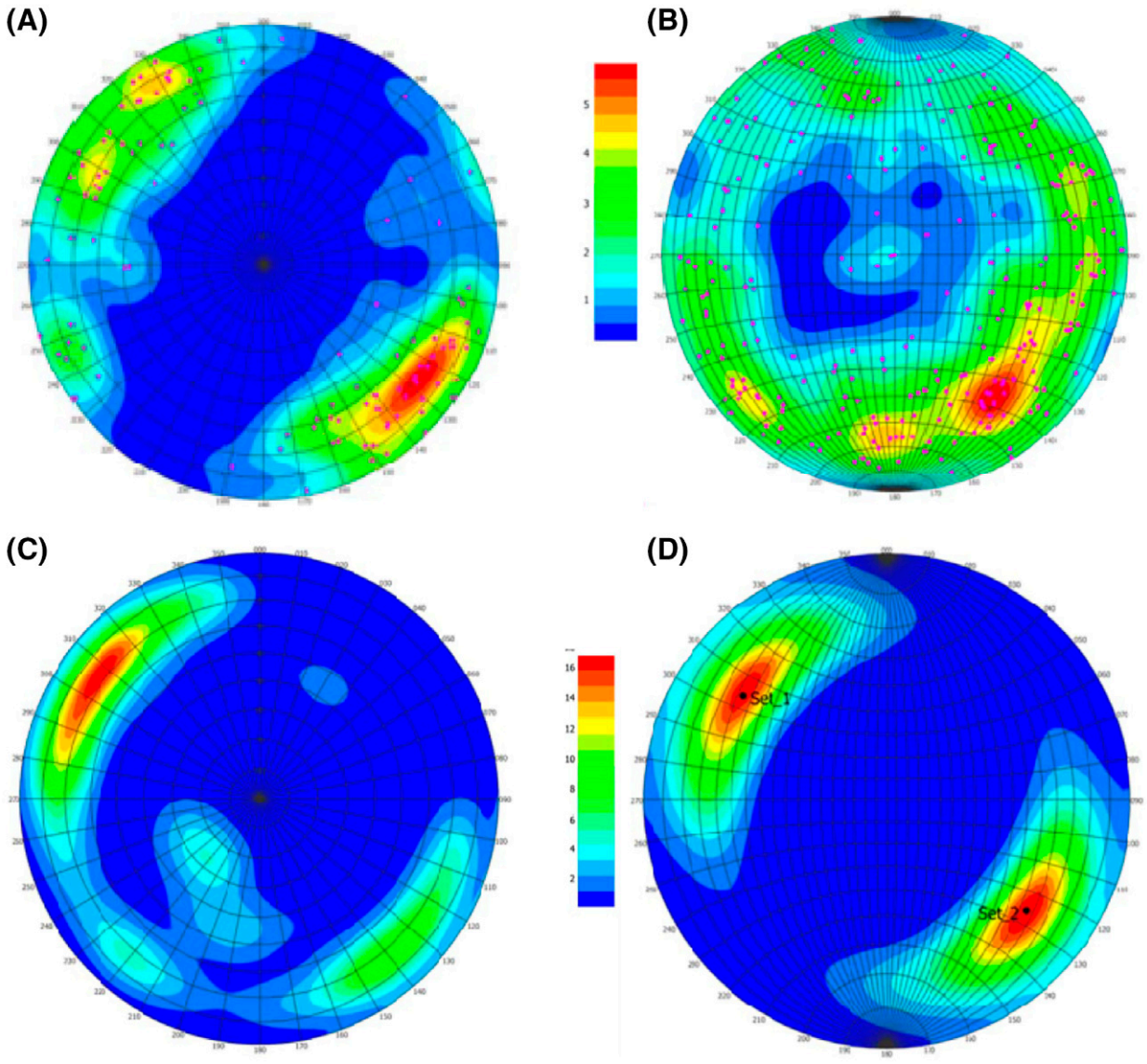

Figure S2. Lower hemisphere, equal-area stereoplots of poles to faults from Horne et al. (2020) used to geometrically condition faults in the discrete fracture network (DFN) model. (A) Faults from the Lhoist quarry outcrop. (B) Faults from the Hoover Point outcrop. (C) Faults from the Fort Worth Basin subsurface from literature. (D) Faults in the Llano Uplift from published maps. See Figure 3 in the main text for location of Lhoist and Hover Point outcrops.

intensity was conditioned to correlate linearly with the heave. The absolute fracture intensity was based on the fault data from the Lhoist and Hover Point outcrops (Figure 3) which are dominated by the smaller background faults, and represents a volumetric conductive fault intensity expressed as the surface area of the faults per unit volume of formation, or P_{32}. The volumetric intensity P_{32} is approximately 10^{-3} ft^2/ft^3.

The size range of the stochastic faults was selected to represent the smaller faults not observed in the framework fault data. Figure S7B shows the size-intensity relationship for the framework faults (orange curve). A break exists in the slope of the orange curve data around 30,000 m. Using this slope break as an upper bound, the stochastic faults were restricted to a maximum of 30,000 m, the result of which is shown by the green line. Some overlap occurs, but the majority of faults greater than 30,000 m are in the framework fault set, and the majority of faults below this cutoff are in the stochastic set.

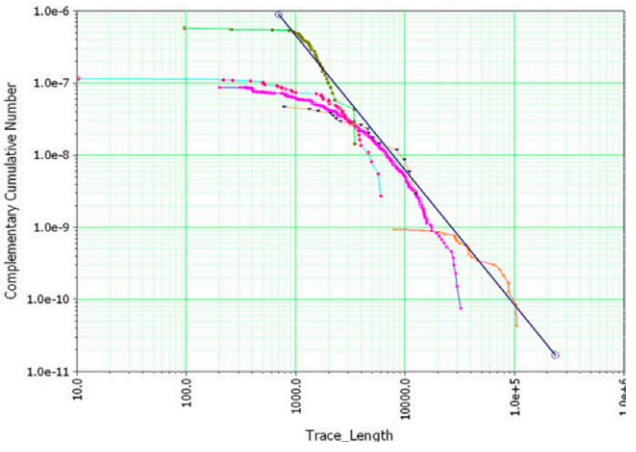

Figure S3. Area-normalized complementary cumulative trace number versus measured trace length (m) for the Llano Uplift fault traces (purple line purple dots), Boonsville fault traces (green line green dots), Venus fault traces (blue line pink dots), Khatiwada fault traces (orange line blue dots), Ewing fault traces (orange line orange dots). See Figure 3 in the main text for location of the volumes from which fault traces are extracted. The size-intensity model for the dominant NE fault set direction conforms to a Power law distribution, $C = \left(\frac{T_{min}}{T}\right)^{-12.62}$, where C is complementary cumulative trace number, $T_{min} = 565$ m is minimum trace length from known measurements, and T is the length of traces of interest. Since larger faults have a higher probability of intersecting a surface such as an outcrop face, the outcrop data has a bias. The bias has the effect of changing the exponent in the equation by a factor of 1.0, such that the exponent for the parent fault population would be −2.62 (La Pointe, 2002).

The spatial pattern of fault size (trace length) for stochastic faults is generated following a Power law model (Figure S7B), assuming minimum fault length of approximately 3000 m, maximum fault length of 30,000 m, and aspect ratio of 10:1. The size-aperture relationship was calibrated from the HWY67 test simulation results and the permeability computed from the aperture.

The aperture and permeability of the background stochastic faults depended upon fault size, and were based on the well test matching for the HWY67 test. The function for aperture, e, was found to be $e = 0.1255 \times \log_{10}(EquivRadius)$ where both e and $EquivRadius$ are in feet. The function for permeability, k_f, is a function of aperture, e, and was found to be $k_f = 4105.85 \times e^{1.5}$ where k_f is in md. Figure S8 shows the resultant upscaled permeability for the model consisting of both the step 1 framework faults and the step 2 stochastic faults.

C. WORKFLOW TO POPULATE MODEL CELLS WITH POROSITY AND PERMEABILITY INFORMATION

In addition to the important fault and fracture input, the workflow uses interpretation of petrophysical well logs and from injection wells tests (Figure S9). Both the porosity and permeability matrix fields are generated based on the petrophysical interpretation of 46 wells (Smye et al., 2019). The locations of these wells are somewhat biased toward the western side of the flow model where there is conventional production from the EBG. No physical core data are publicly available for the EBG in the AOI; therefore, porosity was calculated from neutron-density logs. Porosity values estimated from well logs show a preferential spatial trend in the northeast-southwest parallel to the direction of faulting suggesting that fractures and small faults are widespread and contribute significantly to the total porosity. The average porosity varies by layer (Table 2) with a global average (not including the basement) of 3.5%. Most cells have porosity values between 1% and 6% but locally porosity can be larger than 10%. The basal G layer that contains a high percentage of clastics in its southern half has a higher average porosity of 5.5%.

The permeability field that we implement results from the superposition of three contributions: rock matrix, which includes fractures and small faults that are very close to, or intersect, the wellbores as captured by the bulk behavior of the neutron-density logs; framework faults (step 1 from Section B); and stochastically implemented meso-scale faults (step 2 from Section B) (Tables 1, 2). Given our inability to calibrate log-derived permeability with physical tests on core material, we derived a "permeability index" that was calculated consistently using the logs and was then scaled dynamically, primarily using wellhead pressure history data as described below. The initial scaling of the permeability index was obtained by distributing matrix permeability against porosity, applying Lucia class 2 transform (Lucia, 2007) related to grainstone carbonates (Loucks and Ruppel, 2007) (Figure S9).

The petrophysical analysis and porosity transforms provided permeability index values every 0.5 ft (15 cm) in each well. The northeast-southwest grain related to the main structural orientation is again revealed by a geostatistical analysis and translates in an anisotropic

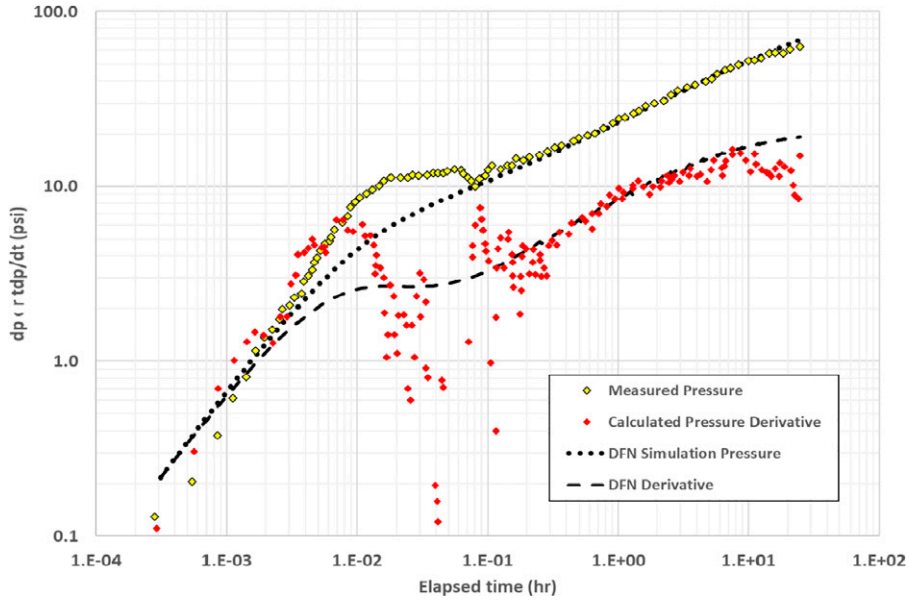

Figure S4. Discrete fracture network (DFN) simulation match to the Briar1 well test. Pressure deviations from static level are measured (dp), and the time derivative is computed (dp/dt).

matrix permeability index field with a preferential northeast-southwest direction. A variable-value multiplier is then applied to the permeability index to obtain the actual matrix permeability field. Multiplier values vary by several orders of magnitude. Finding the parameters of the multiplier function (second-order polynomial of log of permeability) is part of the calibration process. The upscaled matrix permeability field is complemented by local permeability values inferred from injection rate and pressure at injection

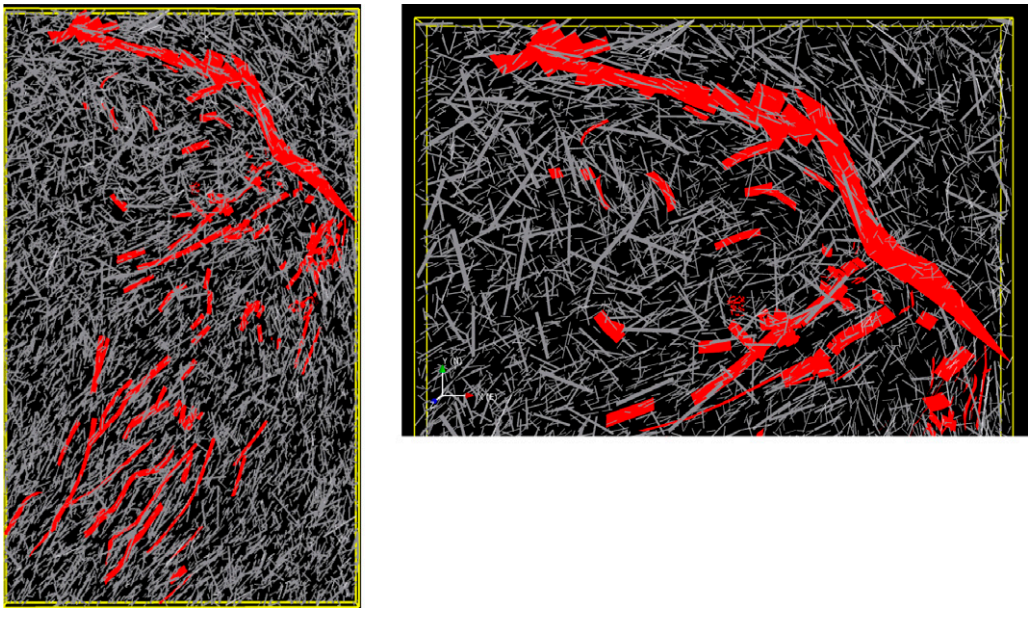

Figure S5. The two steps in discrete fracture network fault model generation are shown. The first step consists of only the large framework faults, shown in red. The second step is the addition of the background stochastic fault set, shown in gray. The image on the left shows the entire Fort Worth Basin model region, whereas the image on the right shows an enlargement of the northern part of the model, revealing detail of the fault size, intensity, and orientation.

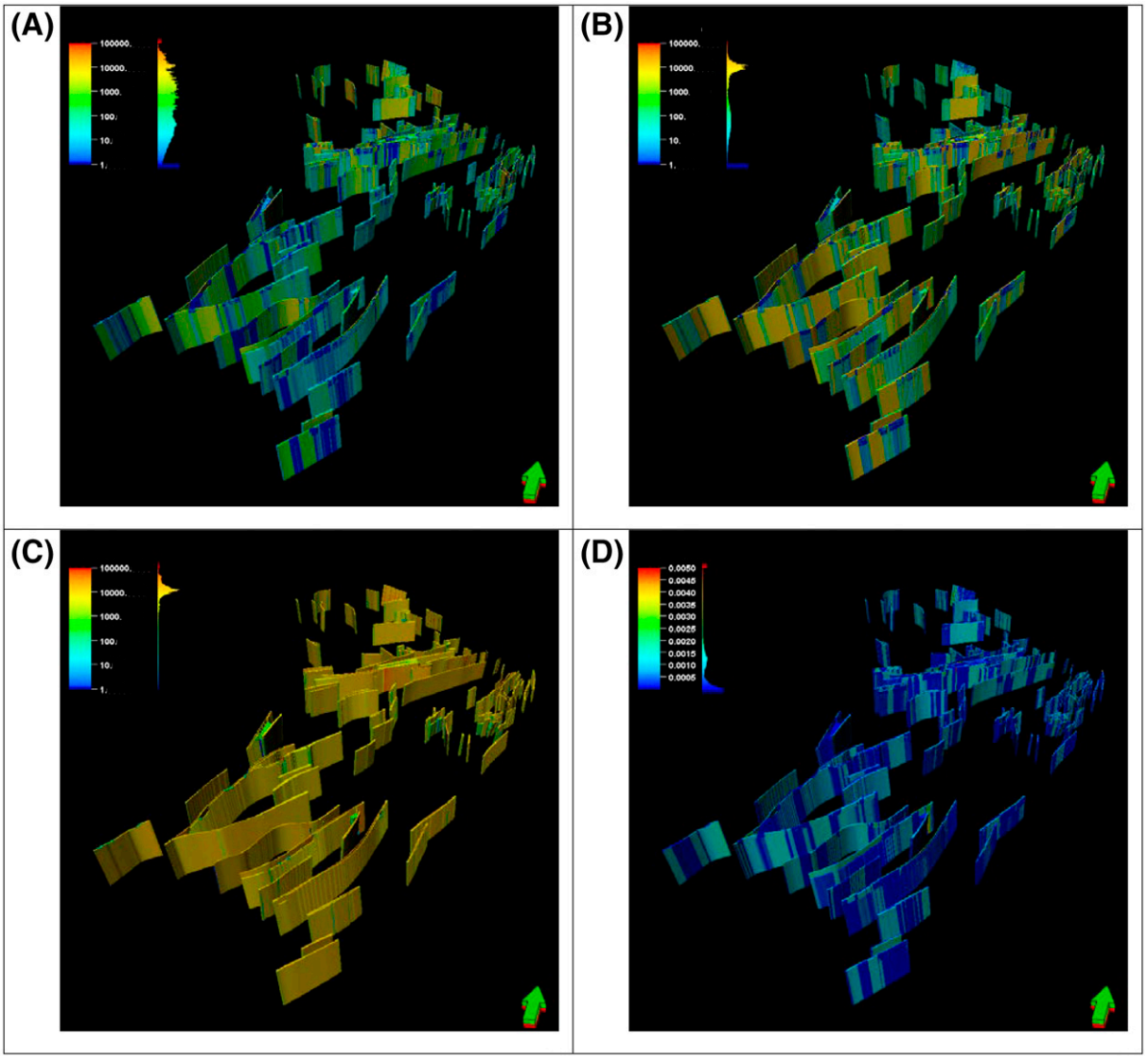

Figure S6. Upscaled fault permeability (in md) in the three major orthogonal directions and porosity ([-]) of framework faults at the end of the first step (Petrel screen captures). (A) Fault permeability in I direction, (B) fault permeability in J direction, (C) fault permeability in z direction, and (D) fault porosity.

well locations (data from a total of 106 out of 127 wells were judged as having accurate data). The latter data set lacks the vertical resolution of the petrophysical study but reflects the permeability that accommodates the injection rate and wellhead pressure including the impact of fractures and small faults. It is also used to guide and constrain the range of values of the matrix permeability of the codomain of the multiplier function (spanning 4 orders of magnitude) constructed from the matrix permeability index domain (spanning 10+ orders of magnitude). Making use of the static petrophysical log information with fine vertical resolution, and field dynamic data of fractured carbonate, we obtained 138 wells with calculated permeability to perform a geostatistical analysis (Figure S9). The final permeability field is then generated by cokriging with porosity. Average matrix permeability by layer varies within a limited range and global matrix permeability is ~45 md. Typical values are between 1 and 200 md with no value higher than 1000 md (Figure 1). Basement matrix permeability is assumed very low. Grid cells values are drawn randomly from a lognormal

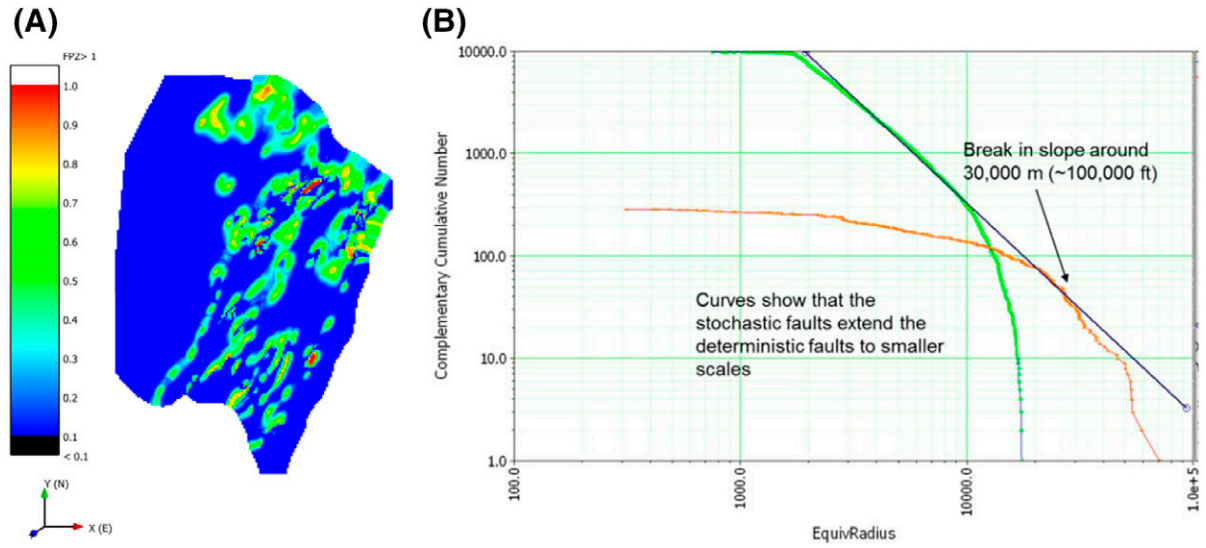

Figure S7. (A) Normalized fault heave around the major faults where a value of 1.0 represented the largest estimated heave and 0.0 represent no estimated heave; (B) Power law representation of major fault trace lengths (feet) versus count. The orange curve is the data set from major faults, showing break in slope at approximately 30,000 m (~100,000 ft).

distribution (mean at 200 nd and standard deviation at 100 nd) and superimposed at the major faults with the major fault permeability which is a tenth of that in the EBG. Using the Petrel software (version 2018.2), well-log and fault data were upscaled to the geomodel grid cell and extended by layer throughout the entire grid using standard geostatistical modeling.

The color-coded outlines of the process boxes correspond to the illustrative function plot with the same colors at the top of the figures: (1) illustrates geostatistical analysis of EBG E layer porosity field; (2) plots the logarithmic multiplier function from permeability index to the desired range of matrix permeability; (3) indicates the lognormal distribution of permeability of one injector well with permeability estimated at k0; and (4) shows the permeability index transformed matrix permeability (left plot) and the scaled permeability log (right plot).

D. IMPLEMENTATION OF WATER PRODUCTION THROUGH BARNETT WELLS

To quantify the importance of the mechanism of withdrawing water from the EBG through gas producing wells (Figure 4), the approach taken here was to assess the gas-water ratio (GWR) through time. In a typical Barnett well, both water and gas production would exhibit similar decline curves with a commonly increasing GWR ratio (less water produced relatively to gas). However, if the well is connected to a large source of water such as the EBG via hydraulic fractures that extended downward, the GWR would decrease because of the declining gas production while still maintaining relatively high water production. We have investigated the GWR history of Barnett wells through a statistical analysis of the percentile distribution. Unlike oil and gas production, which is reported monthly, there are no requirements for reporting of produced water. However, wells are required to be periodically subjected to production tests at the end of which all produced fluid volumes (including water) must be reported. This commonly occurs annually. Although there is a limited number of useable test time series, combining all tests performed within a given quarter following completion of the entire well population yields estimates of GWR percentiles for the quarter. Examining curves of GWR percentile through time (on a quarterly basis) reveals that (1) in the footprint where the Viola-Simpson Formations (Fms). underlie the Barnett Shale, all percentiles behave similarly with a GWR increasing with time, consistent with the expected behavior; and (2) outside of the footprint of the Viola-Simpson Fms., the tenth

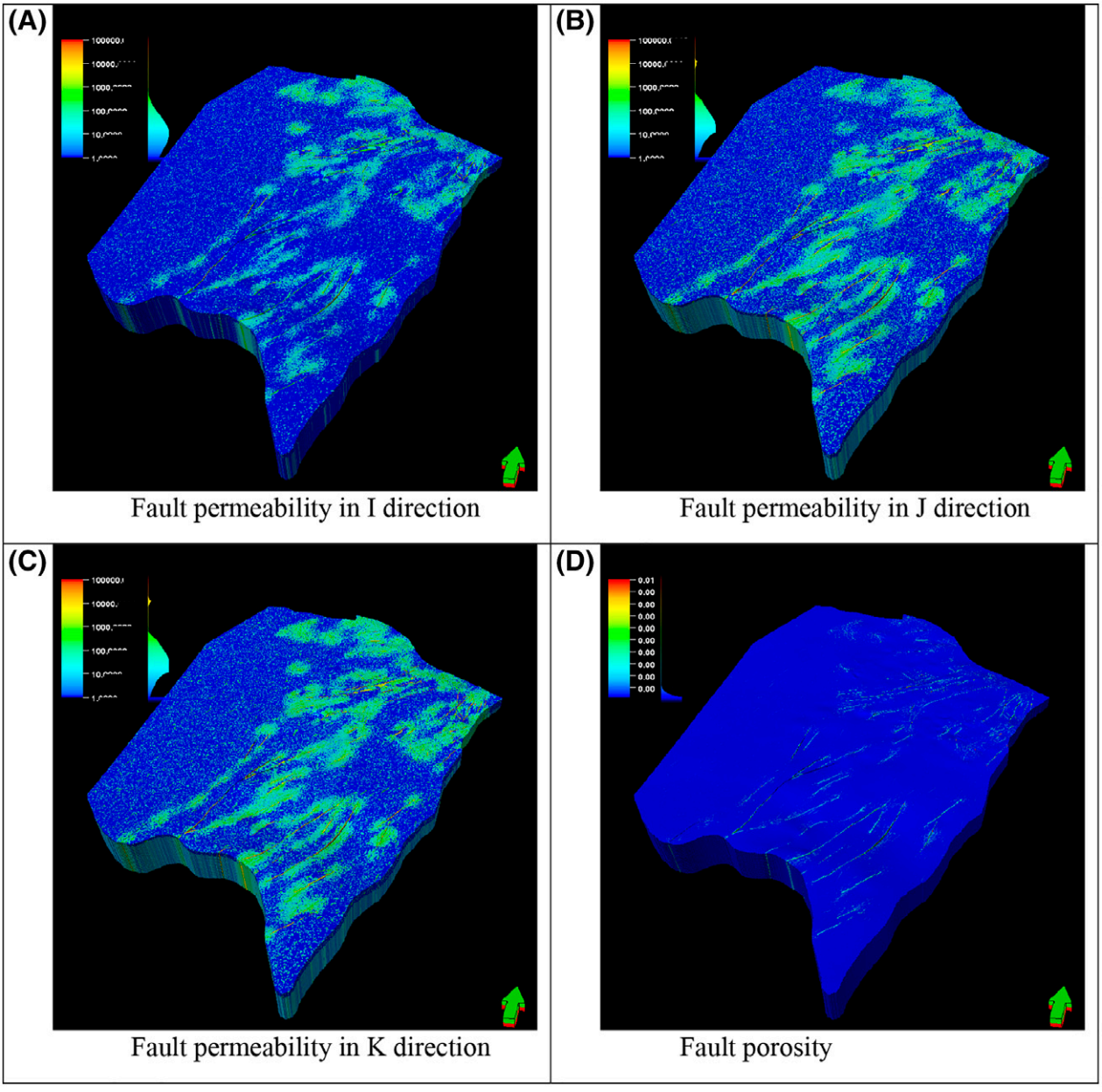

Figure S8. Upscaled fault permeability (millidarcys) in the three major orthogonal directions and porosity ([-]) of both the deterministic framework step and the stochastic faults from the second step.

percentile and below shows a decreasing GWR with time, suggesting connectivity to, and withdrawal from, the EBG. We then used estimates of water production from IHS, combined with the known monthly gas production, to estimate the monthly GWR for each well. A linearly sliding scaling factor is then applied to these data points outside of the Viola-Simpson Fms. and with a GWR lower than that of the 10th percentile (GWR of 8.0 MCF/bbl [1.3×10^3 m^3/m^3] for vertical wells and 3.2 MCF/bbl [0.57×10^3 m^3/m^3]) for horizontal wells. A factor of 0 is given to the water production of monthly production falling exactly on the 10th percentile (no water production from EBG), whereas a factor of 1 is given to the limiting case of 0th percentile (all water produced comes from the EBG). Note that gas produced from Barnett Shale wells is not modeled; however, to account for coproduced water from the EBG, pseudo–water wells are added to the

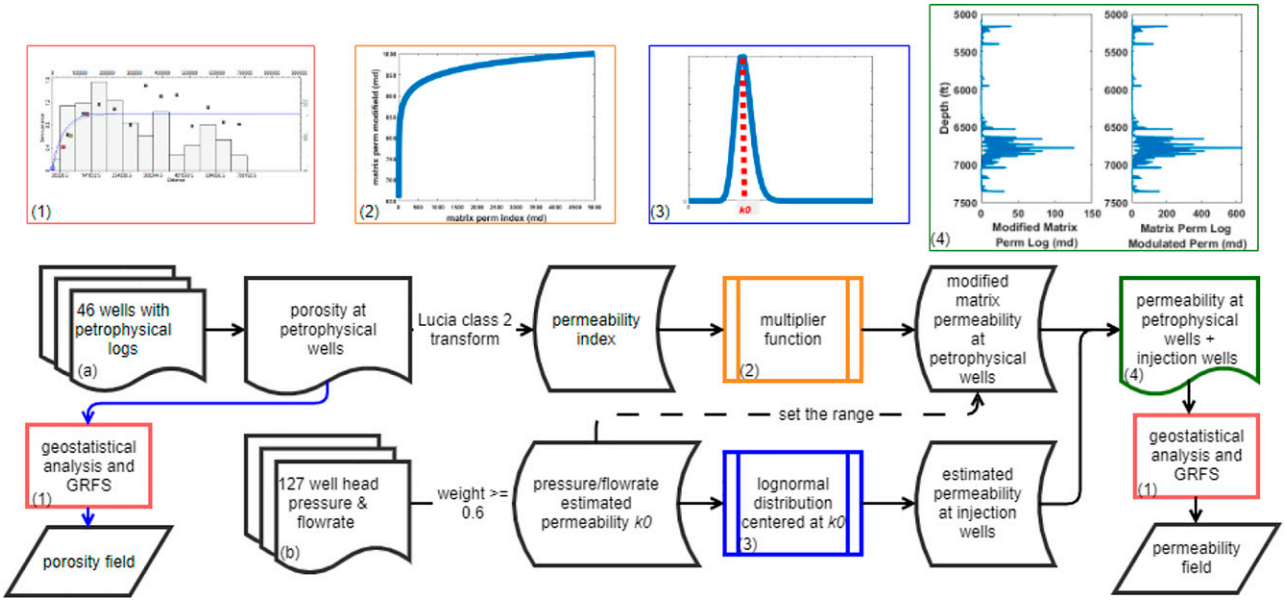

Figure S9. Workflow used to populate the model porosity and permeability fields. Porosity is first derived from 46 petrophysical wells and then its basin-scale field values are generated in Petrel through geostatistical analysis and Gaussian Random Function Simulation (GRFS). Permeability matrix values are derived from two sources: (a) porosity values at the 46 petrophysical wells according to Lucia class 2 transform for carbonate (Lucia, 2007); they yield a permeability index that ranks the permeability values relative to each other, to which a logarithmic multiplier function is applied to obtain the matrix permeability at the location of the petrophysical wells that accounts for the impact of fractures and small faults; (b) estimates of permeability (*k0*) from well head pressure and flowrate history from the 103 injection wells displaying data of sufficient quality (out of a total of 127 wells), that is, with a weight $\geq$0.6; permeability values are then generated according to a lognormal distribution centered on *k0* at the location of each injection well. Note that these field estimates naturally account for fractures and small faults. Then the permeability values from the 46 petrophysical wells and the 103 injection wells are merged into 138 permeability estimation wells (some petrophysical wells and injection wells are coincident). Eventually, final permeability matrix values are generated through geostatistical analysis and GRFS.

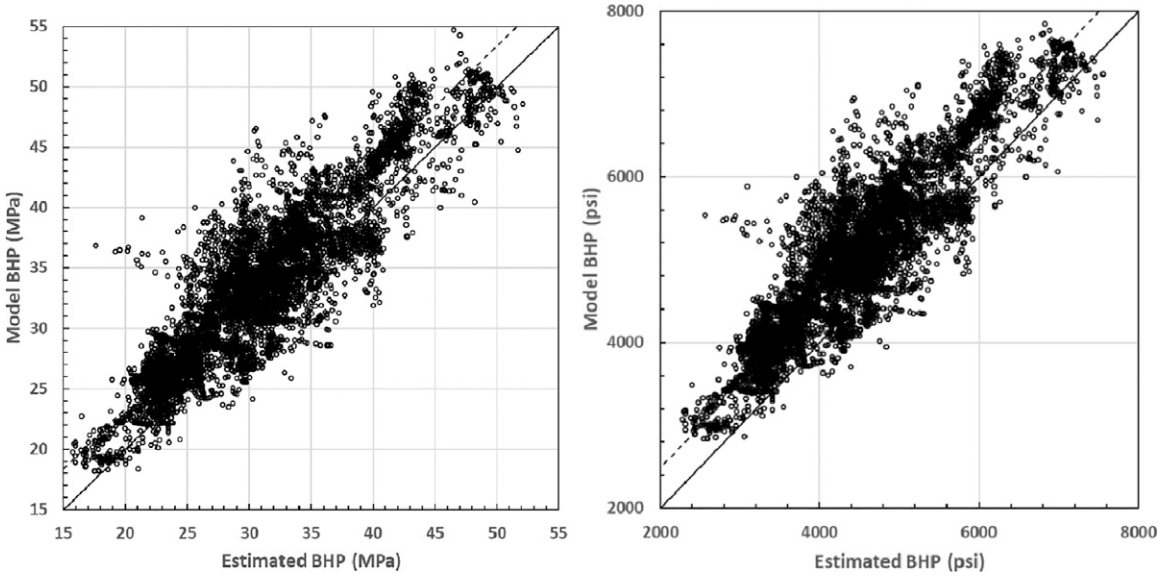

Figure S10. Crossplot of estimated (converted from surface) versus model bottomhole pressure (BHP), all relevant monthly values included. A total of 105 wells have from 9 to 143 useful monthly pressure measurements (41 wells with all data points with a weight of 0.6, 29 wells with all data points with a weight of 1, and 35 wells with mixed weight). Monthly pressure measurements with a lower weight are not included. 58% of the 7823 estimated pressure data points have a given weight of 1. Identical plots in megapascals and pounds per square inch units (1 MPa = 145 psi).

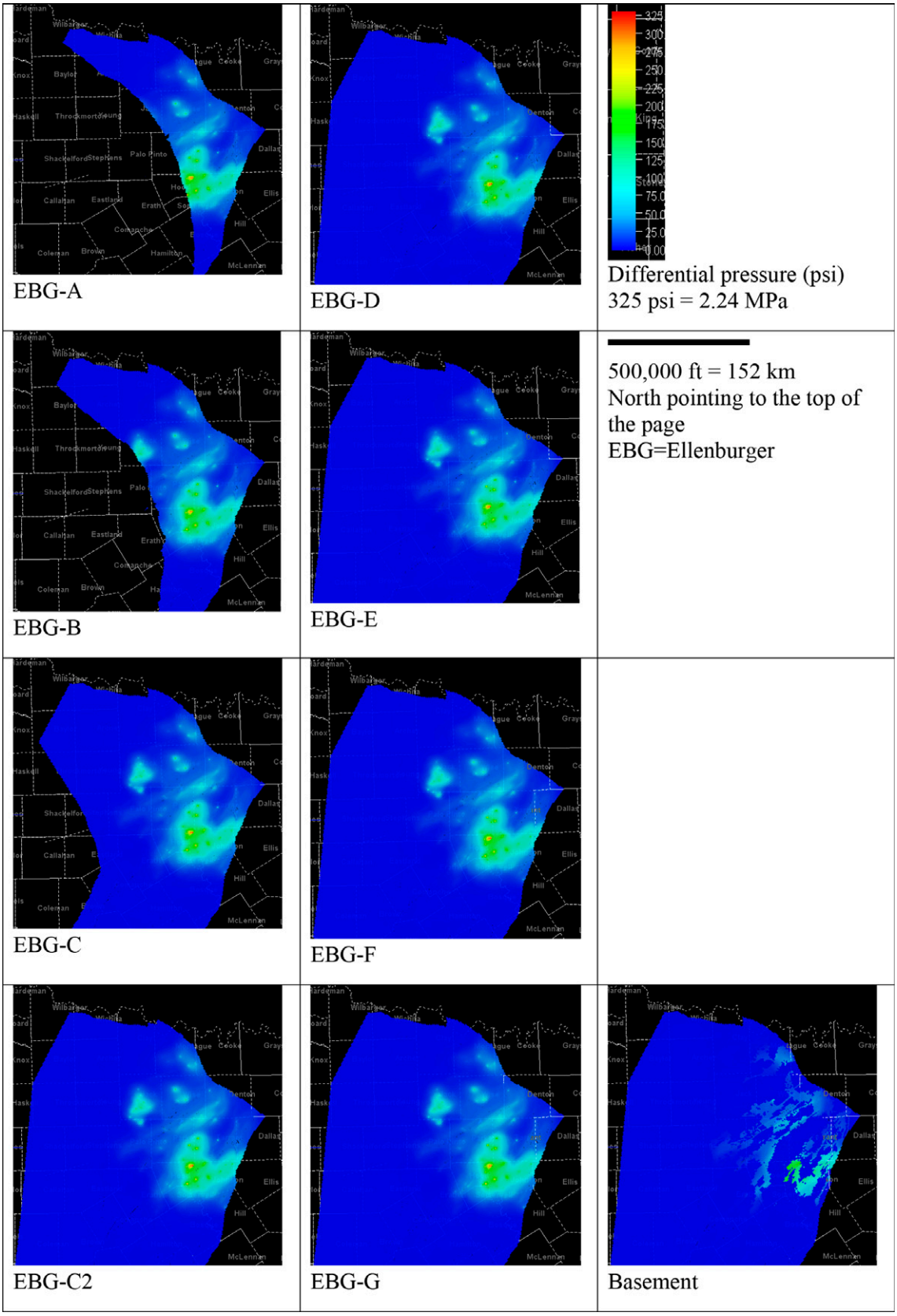

Figure S11. Pressure differentials in all layers at the end of the base case run (January 2019). The differentials are similar in all layers (A, B, C, C2, D, E, F, G) but the basement.

model that withdraw water from whichever layer is in directly under the unconformity. We assigned only one water production well per cell whose rate is the sum of all the relevant Barnett Shale water production wells present in the cell (per their wellhead location). Although this process is imperfect because of the gross nature of our data estimation scheme and underlying inaccuracies in the available data, we believe this accounts for the important effect of coproduced water. We have attempted to minimize these potential errors by thoroughly screening the input data and correcting it as possible. We believe their impact is further minimized by the relatively large size of the model cells which dilutes the impact of these randomly distributed errors by combining several Barnett gas wells in a given cell. A geostatistical analysis showed that a strong nugget effect (~50% of variance) characterizes the GWR's when calculated at several elapsed times since completion with a range similar to the cell size, that is, random for all practical purposes.

E. CALIBRATION

Calibration Results

The calibration results are presented in Figure S10.

Model Calibration Data—Injection Pressure

Injection pressures of SWD wells as measured at the surface range from ~0 psi to over 3000 psi (20.4 MPa). Conversion to downhole pressure was done through an algorithm developed for this study and validated by comparison to a simpler algorithm that is integrated in the commercial modeling software CMG-STARS and by similar calculations presented elsewhere (e.g., Environmental Protection Agency, 2014). The algorithm considers the well completion type (perforated casing or openhole), its dimensions (data from IHS Enerdeq), and assumptions about the material (friction factors of casings and tubing). Many details should be considered when handling this conversion related to operational practices, such as injection interval length and vertical location through time and wells changing owners and how they relate to the reported monthly surface pressures. More importantly, it also suggests that monthly average injection pressure data do not deviate too much from the actual instantaneous pressures. Monthly average pressures must be reported to the state regulator by operators. However, many reported data are clearly inaccurate, for example, constant pressure for years independent of variations in the flow rate. Other presumably accurate pressure data include processes not necessarily included in the model. For example, an increase in injected volume at a lower pressure may mean that the operator moved to a different interval in the well or that the injection interval underwent a workover to improve its performance (change of skin factor, not captured in the model). We attempted to adjust for this in all cases possible. The injection data were screened, sorted, and given a subjective rating from 0 to 1, with 0 reflecting clearly inaccurate data to 1 for data in which pressure varied consistently with the injection rate. Key wells with high ratings were used to inform the permeability field as described earlier.

Additional Results

Typical model results are presented in Figure S11 (differential pressure [ΔP] in all layers at the end of the run in 2019) and Figure S12 (ΔP in the bottom layer in 2005, 2010, 2015, and 2019). The impact and behavior of framework faults is explained in Figure S13.

F. SENSITIVITY ANALYSIS AND DISCUSSION

Model Parameter Sensitivity Analysis

A sensitivity analysis is performed on parameters known to impact reservoir pressure behavior and on elements more specific to this case study (basement, Barnett Shale). Each parameter is varied individually with no effort to include cross-correlation effects (Figure S14). The long transient leading to system equilibrium is run in each case before the start of injection. Permeability, porosity, compressibility, and formation salinity are varied to reasonably but unlikely end members on either side of the values retained for the base case (Table 2). Results of the analyses are evaluated through several simple metrics: (1) an illustrative value of the maximum ΔP between start of injection and last time step; rather than the absolute

largest value of all cells, the 99th and 95th percentiles of the cells sorted in increasing ΔP are chosen to avoid outlier effects, (2) sum across cells of the squared difference between ΔP given in a sensitivity run and ΔP of the base case; sum is performed on all cells in the core area up to the 95th or 99th percentile as given in the base case (equation 1), and (3) the misfit value computed as the sum of the square differences between computed bottomhole pressures and model results at selected injection wells (weigh = 1) and at the same monthly time period (equation 2).

$$1/n\sum_{cell=1}^{cell=95th\ or\ 99th\ percentile}\left(\Delta P_{(i,sensitivity\ case)}-\Delta P_{(i,base\ case)}\right)^2 \quad (1)$$

$$1/N\sum_{well\ 1}^{well\ n}\sum_{j=1}^{j=\text{all well } i \text{ data points}}\left(P_{(i,j,\text{model})}-P_{(i,j,estimated\ calibration\ data)}\right)^2 \quad (2)$$

Conceptual Model Sensitivity Analysis

Barnett Gas as a Compressible Cushion

The potentially high compressibility of the Barnett Shale (rock and contained fluids) can similarly attenuate pressure increase in the EBG. Assuming total compressibility C_t of a multicomponent system is additive and weighted by their volumetric fractions ($C_t = C_{por} + S_wC_w + S_gC_g$), where C_{por} is the pore compressibility, S_w and S_g are water and gas saturation, respectively, and C_w and C_g are water and gas compressibility, respectively, it will be dominated by the compressibility of the gas or supercritical phase relative to that of the rock and water. For an ideal gas, a simple derivation shows that compressibility is the inverse of pressure. Nonideal gases or supercritical fluids are generally less compressible, and for methane, compressibility is within a factor 2 or less of the inverse of pressure. Compressibility of the total system is then in the 20–40 GPa^{-1} range, that is, approximately two orders of magnitude higher than that of water at the same conditions.

Gas Production from the Barnett

Gas production in the Barnett can potentially create a pressure depleted volume that would extend into the EBG and mitigate the pressure increase related to water injection, with the caveat that areas of gas production and water injection may not fully overlap. To approximately test the impact of gas production on EBG pressure distribution in our single-phase model, we need to convert gas production into equivalent water production. However, a simple volumetric conversion is not correct to simulate the impacts on the pressure distribution away from the production zone. We follow the steps described in Hosseini and Nicot (2012) to achieve the correct results. They proposed a method to handle the impact on pressure of relatively distant far field hydrocarbon production (Barnett in this case) on a near-field AOI (EBG) in a single-phase flow modeling construct. It consists of (1) scaling the hydrocarbon-producing area permeability so that its diffusivity (ratio of permeability to compressibility times viscosity) does not change when replaced with water; and (2) scaling the hydrocarbon production (reservoir conditions) by the ratio of compressibility values. We neglect produced water production from the Barnett by noting that the volumes are similar to HF volumes (Nicot et al., 2014); we assume they cancel each other out (i.e., approximately same water volumes in and out).

We approximately modeled the impact of the Barnett Shale by adding two hypothetical Barnett-like constant-thickness layers on the top of the EBG, neglecting the presence of the Viola-Simpson. A shallower 250-ft (76-m)-thick top layer (C1) representing the section of the Barnett undergoing HF stimulation and a deeper 50-ft (15-m) bottom layer (C2) representing an unaffected buffer between the top of the EBG and the stimulated interval (Table S2). We assumed that layer C1 is actively producing and that its permeability has been considerably enhanced through HF to a value of 10 md, whereas C2 permeability is that of the Barnett set at 100 nd (Cipolla et al., 2010; Heller et al., 2014; Bhandari et al., 2015; Cronin et al., 2016; Edwards and Celia, 2018; Eftekhari et al., 2018; Chen et al., 2020; L. Sivila, 2017, personal communication) (Table S2). Porosity and compressibility of both C1 and C2 are assumed identical and set at 6% (aforementioned references) and 4×10^{-6} psi^{-1} (0.6 GPa^{-1}) (Hakso and Zoback, 2019), in agreement with the cited literature and supported by the assessment of the 46 petrophysical logs and those presented in Waters et al. (2011).

Following Hosseini and Nicot (2012) leads to ensuring that diffusivity of the actual and water-only systems is identical and translates into a modified permeability of C1 approximately equaling one-third

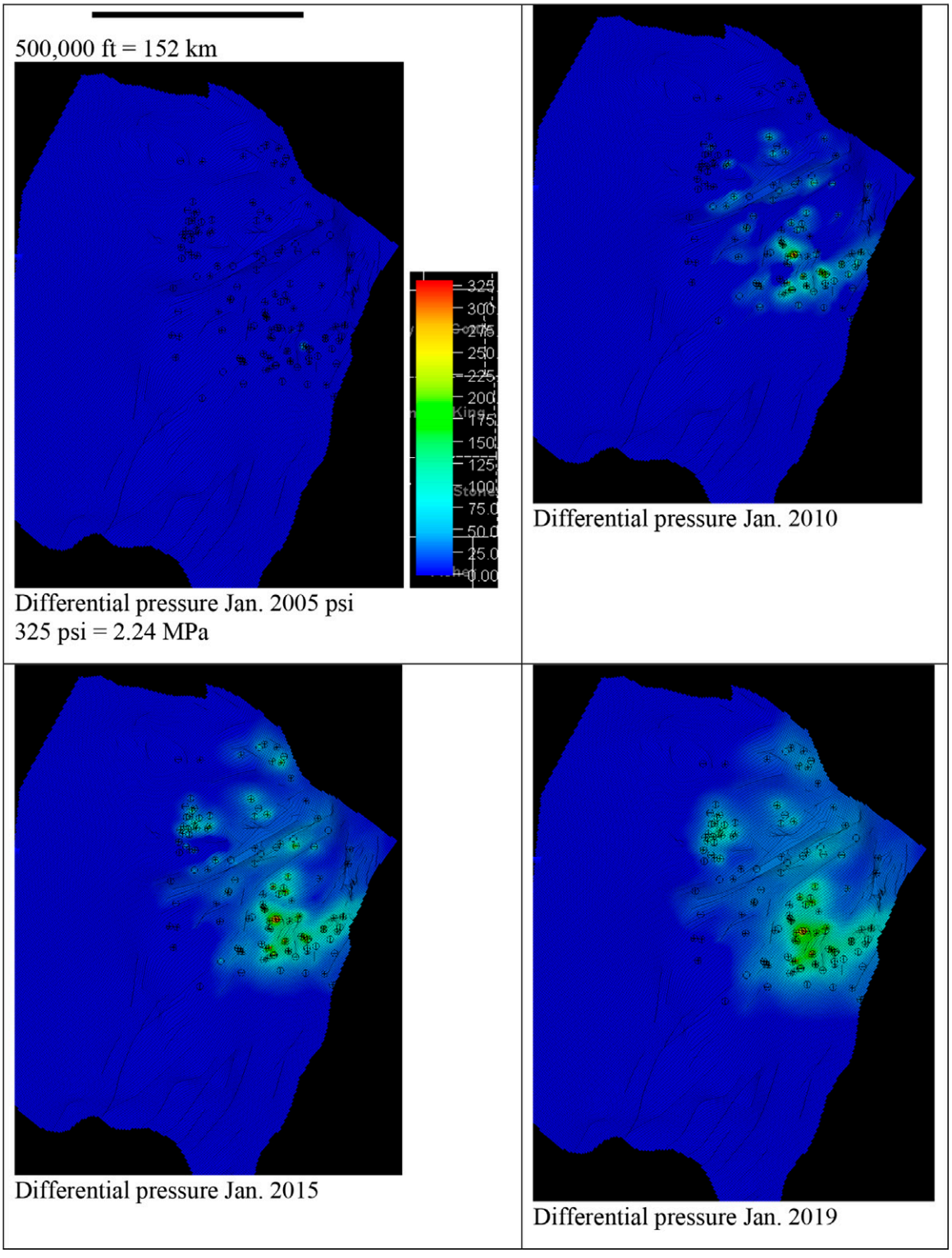

Figure S12. History of pressure differential in the Ellenburger-G layer. Jan. = January.

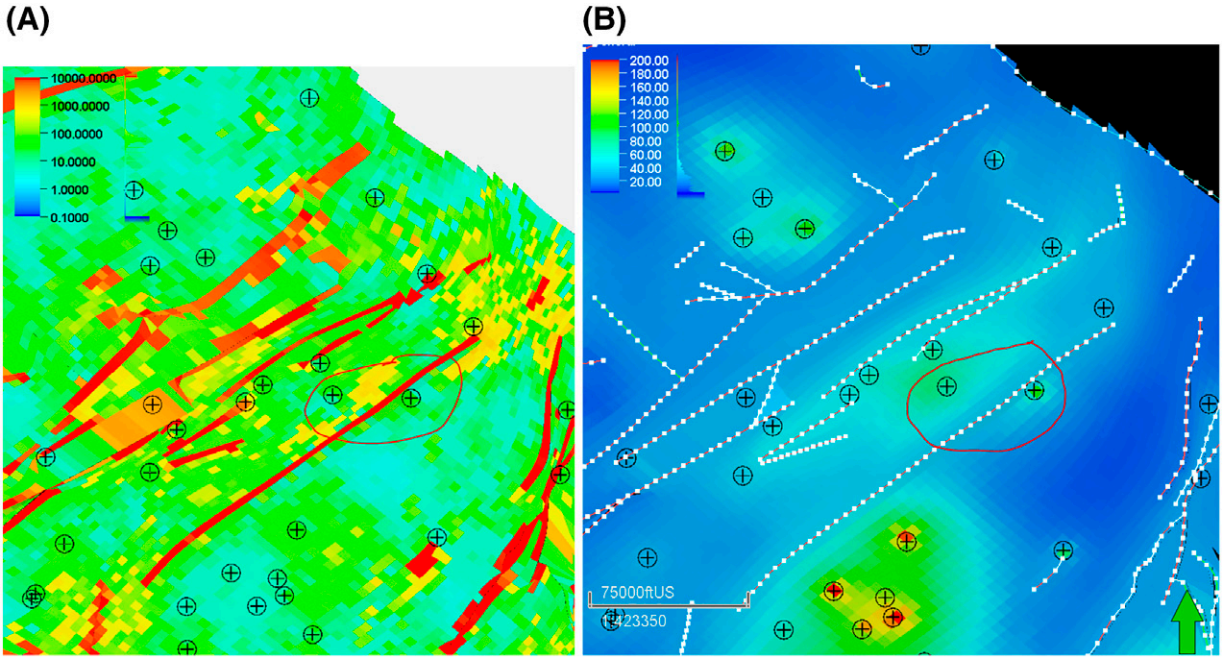

Figure S13. Illustration of the compartmentalization of the system with major faults as boundaries. They limit interferences between wells because of their high permeability. Permeability map of the northern section of the model is shown in (A) (Ellenburger layer G in northeast-southwest direction). Deep red lines indicate the very high permeability along the major faults (permeability scale from 0.1 to 10,000 md); zones with higher fracture density are shown in yellow/orange whereas zones with mostly matrix permeability, away from the main fault zones, appear green/blue. (B) Pressure increase (in pounds per square inch; 100 psi = 0.69 MPa) from start of injection to last modeled step (pressure differential scale from 20 to 200 psi −0.14 to 1.4 MPa). The same framework faults are represented in dotted white lines. The two panels are at the same scale and the area circled with a thin red line includes the same two injection wells (displayed as circled pluses). The circled area in (B) shows a clear separation of pressure increase between the two injectors, whereas (A) shows the permeability values between the two wells are as high as a couple of hundreds of md. The two injectors would display a connected pressure increase area if the very high permeable fault in between did not evacuate some of the pressure increase.

of that of the actual value computed as follows; viscosity ratio of brine/supercritical gas is approximated at 0.2×10^{-3} Pa.s/0.2×10^{-4} Pa.s = 10, whereas compressibility of the single-phase system to that of the actual system can be approximately computed as 1/27.2 (Table S2). Relative permeability ratio gas/brine is assumed to be 0.9. The product of these ratios is ~0.33. Implementing the second step of Hosseini and Nicot (2012) leads to recognizing that total compressibility of the original Barnett system including gas at almost full saturation is

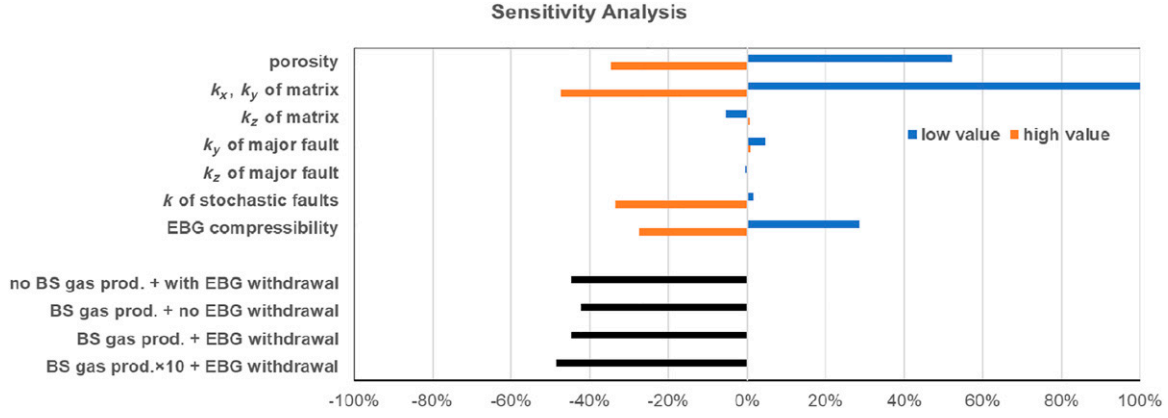

Figure S14. Summary of sensitivity analysis expressed as percentage change of the 99th percentile of pressure increase (all cells included) (Table S1). BS = Barnett Shale; EBG = Ellenburger; k = change in the three directions at the same time; k_x, k_y, k_z = permeability in the three orthogonal directions (x, y, z); prod. = production.

approximately 27.2 times that of a system with only water, translating into a production rate from layer C1 reduced volume-wise by a factor of 27.2. It follows that the needed modifications to approximately shift from the actual multiphase flow system to the single-phase flow model is to use a smaller permeability in layer C1 and a much smaller production rate, also in layer C1. Case A and case B represent variations on the approach by Hosseini and Nicot (2012): C2 either belongs to the "far field" and its nonmodified pore compressibility should be used (case A) or the static gas contributes to the compressibility of the layer (case B). The gas becomes, in essence, part of the rock system whose new pore compressibility becomes $Cr + Sg \times Cg = 25.1$ GPa^{-1} (Table S2).

Conclusions on Variance of the Conceptual Model

Various runs (gas production from C1 and water production from EBG cells in contact with the Barnett Shale, gas production but no water production, no gas production but water production, x10 increase gas production from C1) show that the impact of the Barnett Shale on the ΔP resides mostly in the increased compressibility of layer C2 (Table S1). Our work did not and cannot evaluate rigorously the impact of the Barnett Shale because of the choice of constructing a single-phase model. A multiphase flow model would involve collecting data on many parameters not very well-known at the regional scale and is not truly needed to estimate the ΔP. The simple approach suggests that the low permeability and high compressibility of the hypothetical layer C2 (with no enhanced permeability because of HF) shields the EBG from changes in the production of Barnett Shale (layer C1) and, at the same time, attenuates the pressure buildup in the EBG. Examination of various pressure indicator data sets (IHS Markit, 2019), mud weight and instantaneous pressure shut-in during HF stimulation (e.g., Friedrich and Monson, 2013), confirms that no significant pressure reduction at the regional level in the typically

Table S1. Summary of Selected Sensitivity Analysis Runs

Sensitivity Case	A Factor	A ΔP 99th %	B $\Delta(\Delta P$ 99th), %	C $\Sigma[(\Delta(\Delta P$ 99th))^2]	D Σ $[(\Delta BHP)^2]$	E Factor	E ΔP 99th %	F $\Delta(\Delta P$ 99th), %	G $\Sigma[(\Delta(\Delta P$ 99th))^2]	H $\Sigma[(\Delta BHP)^2]$
Base case	–	159	0	0	0.65	–	159	0	0	0.65
Porosity	/2	242	52	1232	0.68	*2	104	−35	502	0.62
Matrix k_x, k_y	/10	323	103	2164	1.20	*10	84	−47	476	0.55
Matrix k_z	/10	151	−5	12	0.65	*10	160	1	9	0.64
Major fault k_z	/1000	167	5	73	0.67	*1000	160	1	8	0.65
Major fault k_y	/1000	158	−1	0.5	0.65	*1000	159	0	0.02	0.65
Stochastic fault k_x, k_y, k_z	/100	162	2	42	0.69	*100	106	−34	246	0.58
EBG compressibility	/2	204	29	326	0.68	*2	115	−27	290	0.62
No Barnett Shale gas production + EBG water withdrawal		88	−45	–	–	–	–	–	–	–
Barnett Shale gas production + no EBG water withdrawal		92	−42	–	–	–	–	–	–	–
Barnett Shale gas production + EBG water withdrawal		88	−45	–	–	–	–	–	–	–
Barnett Shale gas production ×10 + EBG water withdrawal		82	−49	–	–	–	–	–	–	–

Columns A, B, C, and D address a reduction in the parameter value ("/"), whereas columns E, F, G, and H address an increase in the parameter value ("*"). Columns A and E: ninety-ninth percentile of the pressure change (psi) relative to the pressure distribution before start of injection (1 MPa = 145 psi); Columns B and F: percentage change of column A value compared to the base case; Columns C and G: average of the squared pressure difference (psi^2) between base case and sensitivity case for the cells carrying the bottom 99% pressure change values: Columns D and H: average of the squared difference between model pressure and "data" (estimated bottomhole pressure [BHP]) for all 105 wells and all time steps (10^6 psi^2) (see Figure S10).

Abbreviations: EBG = Ellenburger.

Table S2. Characteristics of the Barnett-Like Layers for the Model Sensitivity Analysis

Sensitivity Case	C1 (Top): Representing Barnett Shale Section Undergoing Hydraulic Fracturing Stimulation	C2 (Bottom): Representing Barnett Shale Section as an Unperturbed Buffer between Ellenburger and Stimulated Section
Set thickness, ft/m	250/76	50/15
Actual properties		
Porosity	6%	6%
Cr, psi^{-1}/GPa^{-1}	$4 \times 10^{-6}/0.6$	$4 \times 10^{-6}/0.6$
Permeability (horizontal *kh* and vertical *kv*)	*kh* = 30 md, *kv* = 30 md	*kh* = 1×10^{-4} md = 100 nd, *kv* = 0.05×10^{-4} md = 5 nd
Isothermal *Cg*	$34\ GPa^{-1}$	
Cw	$\sim 0.3\ GPa^{-1}$	
Sw	0.3	
~*Sg* (nonadsorbed gas)	0.7	
Ct	$Ct = Sw \times Cw + Sg \times Cg + Cr = 24.5\ GPa^{-1}$	
Qgas	*Qgas* at Reservoir Conditions	0
Modified properties		
Action	Equivalent gas production	No flow
Porosity	No change – 6%	No change – 6%
Pore compressibility (psi^{-1}/GPa^{-1})	No change, $4 \times 10^{-6}/0.6$	No change, $4 \times 10^{-6}/0.6$
Modified permeability (horizontal *kh* and vertical *kv*)	*kh* = 10 md, *kv* = 10 md	No change, *kh* = 1×10^{-4} md = 100 nd, *kv* = 0.05×10^{-4} md = 5 nd
Total compressibility ratio = *Ct*/(*Cw*+*Cr*)	~27.2	
Sw	100%	100%
Sg	0%	0%
Qgas-mod	Reservoir Conditions *Qgas* divided by compressibility ratio: *Qgas-mod* = *Qgas*/27.2	0
Case A	As described above	
Case B	The only change is the use of the gas-filled compressibility in layer C2	
Cr mod	No change	*Cr mod* = *Cr*+*Sg*×*Cg* = $25.1\ GPa^{-1}$

Abbreviations: *Cg* = gas compressibility; *Cr* = pore compressibility; *Cr mod* = modified pore compressibility; *Ct* = total compressibility; *Cw* = water compressibility; *kh* = horizontal permeability; *kv* = vertical permeability; *Qgas* = gas production rate; *Qgas-mod*, modified *Qgas*; *Sg* = gas saturation; *Sw* = water saturation.

overpressured Barnett Shale exists; the fraction of gas removed from the Barnett Shale remains small.

REFERENCES CITED

Barnes, V. E., and P. R. Rose, 1981, Geological atlas of Texas, Llano sheet: Austin, Texas, The University of Texas at Austin, Bureau of Economic Geology, scale 1:250,000, 15 p.

Bhandari, A. R., P. B. Flemings, P. J. Polito, M. B. Cronin, and S. L. Bryant, 2015, Anisotropy and stress dependence of permeability in the Barnett Shale: Transport in Porous Media, v. 108, no. 2, p. 393–411, doi:10.1007/s11242-015-0482-0.

Brace, W. F., J. B. Walsh, and W. T. Frangos, 1968, Permeability of granite under high pressure: Journal of Geophysical Research, v. 73, no. 6, p. 2225–2236, doi:10.1029/JB073i006p02225.

Chen, R., X. Xue, J. Park, A. Datta-Gupta, and M. J. King, 2020, New insights into the mechanisms of seismicity in the Azle area, North Texas: Geophysics, v. 85, no. 1, p. EN1–EN15, doi:10.1190/geo2018-0357.1.

Cipolla, C. L., E. P. P. Lolon, J. C. C. Erdle, and B. Rubin, 2010, Reservoir modeling in shale-gas reservoirs: SPE Reservoir Evaluation & Engineering, v. 13, no. 4, p. 638–653, doi:10.2118/125530-PA.

Cronin, M. B., P. B. Flemings, and A. R. Bhandari, 2016, Dual-permeability microstratigraphy in the Barnett Shale: Journal of Petroleum Science Engineering, v. 142, p. 119–128, doi:10.1016/j.petrol.2016.02.003.

Cuong, T. X., and J. K. Warren, 2009, Bach Ho Field, a fractured granitic basement reservoir, Cuu Long Basin, Offshore SE Vietnam: A "buried-hill" play: Journal of

Petroleum Geology, v. 32, no. 2, p. 129–156, doi:10.1111/j.1747-5457.2009.00440.x.

Dershowitz, W. S., and H. H. Herda, 1992, Interpretation of fracture spacing and intensity, *in* J. R. Tillerson and W. Wawersik, eds., Proceedings of the 33rd US Rock Mechanics Symposium, June 3–5, 1992, Santa Fe, New Mexico, p. 757–766.

Edwards, R. W. J., and M. A. Celia, 2018, Shale gas well, hydraulic fracturing, and formation data to support modeling of gas and water flow in shale formations: Water Resources Research, v. 54, p. 3196–3206, doi:10.1002/2017WR022130.

Eftekhari, B., M. Marder, and T. W. Patzek, 2018, Field data provide estimates of effective permeability, fracture spacing, well drainage area and incremental production in gas shales: Journal of Natural Gas Science and Engineering, v. 56, p. 141–151, doi:10.1016/j.jngse.2018.05.027.

Elebiju, O. O., G. R. Keller, and K. J. Marfurt, 2010, Investigation of links between Precambrian basement structure and Paleozoic strata in the Fort Worth Basin, Texas, U.S.A., using high-resolution aeromagnetic (HRAM) data and seismic attributes: Geophysics, v. 75, no. 4, p. B157–B168, doi:10.1190/1.3435939.

Environmental Protection Agency, 2014, Minimizing and managing potential impacts of injection-induced seismicity from class II disposal wells: practical approaches, accessed June 1, 2019, https://www.epa.gov/sites/production/files/2015-08/documents/induced-seismicity-201502.pdf.

Ewing, T. E., 1991, The Tectonic Framework of Texas (and accompanying text): Austin, Texas, Bureau of Economic Geology, The University of Texas at Austin, scale 1:750,000, 4 sheets.

Friedrich, M., and G. Monson, 2013, Two practical methods to determine pore pressure regimes in the Spraberry and Wolfcamp Formations in the Midland Basin: Unconventional Resources Technology Conference, Denver, Colorado, August 12–14, 2013, SPE 168834/URTeC 1582132, p. 2475–2486, doi:10.1190/urtec2013-258.

Hakso, A., and M. Zoback, 2019, The relation between stimulated shear fractures and production in the Barnett Shale: Implications for unconventional oil and gas reservoirs: Geophysics, v. 84, no. 6, p. B461–B469, doi:10.1190/geo2018-0545.1.

Hall, H. N., 1953, Compressibility of reservoir rocks, Petroleum Transactions, AIME, v. 198, p. 309–311.

Hardage, B. A., D. L. Carr, D. E. Lancaster, J. L. Simmons Jr., R. Y. Elphick, V. M. Pendleton, and R. A. Johns, 1996, 3-D seismic evidence of the effects of carbonate karst collapse on overlying clastic stratigraphy and reservoir compartmentalization: Geophysics, v. 61, p. 1336–1350, doi:10.1190/1.1444057.

Heller, R., J. Vermylen, and M. Zoback, 2014, Experimental investigation of matrix permeability of gas shales: AAPG Bulletin, v. 98, no. 5, p. 975–995, doi:10.1306/09231313023.

Hennings, P. H., J.-E. Lund Snee, J. L. Osmond, H. R. DeShon, R. Dommisse, E. Horne, C. Lemons, and M. D. Zoback, 2019, Injection-induced seismicity and fault-slip potential in the Fort Worth Basin, Texas: Bulletin of the Seismological Society of America, v. 109, no. 5, p. 1615–1634, doi:10.1785/0120190017.

Horne, E. A., P. H. Hennings, J. L. Osmond, and H. R. DeShon, 2020, Structural characterization of potentially seismogenic faults in the greater Fort Worth Basin: Interpretation, v. 8, no. 2, p. T323–T347, doi:10.1190/int-2019-0188.1.

Hosseini, S.A., and J.-P. Nicot, 2012, Numerical modeling of a multiphase water-oil-CO_2 system using a water-CO_2 system: Application to the far field of a U.S. Gulf Coast reservoir: International Journal of Greenhouse Gas Control, v. 10, p. 88–99, doi:10.1016/j.ijggc.2012.06.001.

Huang, Y., B. R. Scanlon, J.-P. Nicot, R. C. Reedy, A. R. Dutton, V. A. Kelley, and N. E. Deeds, 2012, Sources of groundwater pumpage in a layered aquifer system in the Upper Gulf coastal plain, USA: Hydrogeology Journal, v. 20, p. 783–796, doi:10.1007/s10040-012-0846-2.

IHS Markit, 2019, IHS Enerdeq Browser download, accessed September 15, 2019, https://penerdeq.ihsenergy.com/thin2/secure/about.jsf.

Khatiwada, M., G. R. Keller, and K. J. Marfurt, 2013, A window into the Proterozoic: Integrating 3D seismic, gravity, and magnetic data to image subbasement structures in the southeast Fort Worth Basin: Interpretation, v. 1, p. T125–T141, doi:10.1190/INT-2013-0041.1.

Kier, R., L. F. J. Brown, P. Harwood, and V. E. Barnes, 1976, Geological atlas of Texas, Brownwood sheet: Austin, Texas, The University of Texas at Austin, Bureau of Economic Geology, scale 1:250,000, 21 p.

Kondash, A. J., E. Albright, and A. Vengosh, 2017, Quantity of flowback and produced waters from unconventional oil and gas exploration: Science of the Total Environment, v. 574, p. 314–321, doi:10.1016/j.scitotenv.2016.09.069.

La Pointe, P. R., 2002, Derivation of parent fracture population statistics from trace length measurements of fractal fracture populations: International Journal of Rock Mechanics and Mining Sciences, v. 39, no. 3, p. 381–388, doi:10.1016/S1365-1609(02)00021-7.

Loucks, R. G., and S. C. Ruppel, 2007, Mississippian Barnett Shale: Lithofacies and depositional setting of a deep-water shale-gas succession in the Fort Worth Basin, Texas: AAPG Bulletin, v. 91, no. 4, p. 579–601, doi:10.1306/11020606059.

Lucia, F. J., 2007, Carbonate reservoir characterization, 2nd ed.: New York, Springer-Verlag, 336 p.

McDonnell, A., R. G. Loucks, and T. Dooley, 2007, Quantifying the origin and geometry of circular sag structures in northern Fort Worth Basin, Texas: Paleocave collapse, pull-apart fault systems, or hydrothermal alteration?: AAPG Bulletin, v. 91, no. 9, p. 1295–1318, doi:10.1306/05170706086.

Nicot, J.-P., A. Gherabati, R. Darvari, and P. Mickler, 2018, Salinity reversal and water freshening in the Eagle Ford Shale, Texas, USA: ACS Earth & Space Chemistry, v. 2, no. 11, p. 1087–1094, doi:10.1021/acsearthspacechem.8b00095.

Nicot, J.-P., B. R. Scanlon, R. C. Reedy, and R. A. Costley, 2014, Source and fate of hydraulic fracturing water in the Barnett Shale: A historical perspective: Environmental Science &

Technology, v. 48, no. 4, p. 2464–2471, doi:10.1021/es404050r.

Oda, M., 1985, Permeability tensor for discontinuous rock masses: Géotechnique, v. 35, no. 4, p. 483–495, doi:10.1680/geot.1985.35.4.483.

Railroad Commission of Texas, 2015a, Docket No. 09-0296410: Austin, Texas, Railroad Commission of Texas Office of General Counsel, accessed October 1, 2019, 45 p., https://www.rrc.texas.gov/resource-center/research/research-queries/imaged-records/how-to-search-oil-andgas-hearings-files/.

Railroad Commission of Texas, 2015b, Docket No. 09-0296411: Austin, Texas, Railroad Commission of Texas Office of General Counsel, accessed October 1, 2019, https://www.rrc.texas.gov/resource-center/research/research-queries/imaged-records/how-to-search-oil-andgas-hearings-files/.

Railroad Commission of Texas, 2015c, Special studies, accessed October 1, 2019, https://www.rrc.state.tx.us/about-us/resource-center/research/special-studies/.

Scanlon, B. R., R. E. Mace, M. E. Barrett, and B. Smith 2003, Can we simulate regional groundwater flow in a karst system using equivalent porous media models? Case study, Barton Springs Edwards aquifer, USA: Journal of Hydrology, v. 276, no. 1–4, p. 137–158, doi:10.1016/S0022-1694(03)00064-7.

Setlur, N., J. M. Sharp Jr., and B. B. Hunt, 2019, Crystalline-rock aquifer system of the Llano Uplift, Central Texas, USA: Hydrogeology Journal, v. 27, p. 2431–2446, doi:10.1007/s10040-019-02000-4.

Shi, J., R. Boghici, W. Kohlrenken, and W. Hutchison, 2016, Minor aquifers of the Llano Uplift region of Texas (Marble Falls, Ellenburger-San Saba, and Hickory): Austin, Texas, Texas Water Development Board, 426 p.

Smye, K. M., C. R. Lemons, R. Eastwood, G. McDaid, and P. H. Hennings, 2019, Stratigraphic architecture and petrophysical characterization of formations for deep disposal in the Fort Worth Basin, Texas: Interpretation, v. 7, no. 4, p. SL1–SL17, doi:10.1190/INT-2018-0195.1.

Standen, A., and R. Ruggiero, 2007, Llano uplift aquifers: Structure and stratigraphy: Austin, Texas, Texas Water Development Board, 426 p.

Texas Water Development Board, 1972, A survey of the subsurface saline water of Texas, volume 1: Dallas, Texas, Texas Water Development Board Report 157, 113 p.

Waters, G. A., R. E. Lewis, and D. C. Bentley, 2011, The effect of mechanical properties anisotropy in the generation of hydraulic fractures in organic shales: Society of Petroleum Engineers Annual Technical Conference and Exhibition, Denver, Colorado, October 30–November 2, 2011, SPE-146776-MS, 25 p., doi:10.2118/146776-MS.

Zhai, G., and M. Shirzaei, 2018, Fluid injection and time-dependent seismic hazard in the Barnett Shale, Texas: Geophysical Research Letters, v. 45, p. 4743–4753, doi:10.1029/2018GL077696.